THERMO-MECHANICAL DYNAMICS ANALYSIS OF SMART FG-GPL NANOCOMPOSITE BEAMS BY DQ-FEM

Mohammed Yassine MAZARI*, **Ismail BENSAID***, **Ahmed SAIMI****, **Abdelmadjid CHEIKH***, **Ihab Eddine HOUALEF***, **Billel HAMZA*****

*IS2M Laboratory, mechanical engineering department, Faculty of Technology, University Abou Bekr Belkaid Tlemcen (UABT), Algeria
**Mechanical Engineering Department, Faculty of Science and Technology, University Belhadj Bouchaib, Ain Temouchent, Algeria
***LaRTFM Laboratory, Department of Mechanical Engineering, National Polytechnic School of Oran Maurice Audin, Oran, Algeria

Mohammedyassine.mazari@univ-tlemcen.dz, bensaidismail@yahoo.fr, ahmedsaimi07@gmail.com, am_cheikh@yahoo.fr, ihabihabeddine1@gmail.com, billel.hamza@enp-oran.dz

received 27 April 2025, revised 24 September 2025, accepted 28 September 2025

Abstract: This study investigates the free vibration behaviour of piezoelectric multi-layered functionally graded nanocomposite beams reinforced with graphene platelets (GPLs) under combined thermal and electrical fields. Different GPLs distribution patterns are considered to enhance the mechanical performance of the material. The effective properties are estimated using the rule of mixtures and the modified Halpin–Tsai model. The equations of motion are derived within the quasi-3D beam theory, accounting for shear deformation and stretching effects. For the numerical solution, the Differential Quadrature Finite Element Method (DQ-FEM) is employed, offering high accuracy and computational efficiency. Results reveal that increasing temperature and applied electric potential reduce the structural stiffness and natural frequencies, with the effect becoming more pronounced at higher GPL contents and piezoelectric coefficients. A comprehensive parametric study demonstrates the influence of GPL distribution, volume fraction, beam geometry, number of layers, and boundary conditions on the vibration response, highlighting the strong coupling between thermal, electrical, and mechanical fields in such smart nanocomposite structures.

Key words: free vibration, Quasi-3D beam theory, DQ-FEM, thermal effect, rule of mixture, graphene reinforced composite beam GPL

1. INTRODUCTION

Composite nanomaterials, such as graphene sheets and carbon nanotube that have been used as reinforcement elements in various materials types, represent some of the most innovative reinforcement techniques available today. Graphene is a material characterized by its excellent electromechanical and thermal properties. Graphene exhibits a tensile strength of approximately 130.5 *GPa* and an elastic modulus exceeding 1 TPa. Its electrical conductivity surpasses that of copper by a factor of 1000 in terms of current carrying capacity. Graphene is composed by a fundamental structure that consists of carbon atoms are organized in a regular hexagonal structure, resembling graphite, but in a different form a single layer one atom thick. Additionally, graphene is exceptionally lightweight a sheet of one square meter has a weight of only 0.77 mg. Due to its exceptional properties and success for enhancing materials, graphene has been employed by researchers in several studies[1],[2] and [3]. Particularly, a number of publications have investigated the use of this material to reinforce structures. The mechanical characteristics of epoxy nanocomposites strengthened with weight fraction 0.1% graphene Nano platelets (*GPLs*) and carbon nanotubes (*CNTs*), respectively, were studied and compared by Rafiee et al. [4]. They discovered that graphene nanocomposites had far greater tensile strength, Young's modulus, and fracture toughness are higher in pure epoxy compared to other materials, and that *GPLs* greatly surpass *CNTs* in terms of enhancing mechanical characteristics. Kundalwal et al. [5] reviewed various micromechanics models to predict the thermomechanical properties of fiber and Nano reinforced composites, highlighting their applicability to advanced materials such as graphene based systems. More recently, studies have shown that graphene not only improves the mechanical performance of nanocomposites but also exhibits piezoelectric behavior due to pores, curvature, and flexoelectric effects. Analytical, numerical, and molecular dynamics models confirm that these effects significantly influence the electromechanical response, making graphene reinforced nanocomposites highly promising for developing lightweight sensors, actuators, and other smart devices. Wu et al. [6] explored the dynamic instability of functionally graded nanocomposite beams reinforced with graphene platelets (*GPLs*) under thermal loading and periodic axial forces. By combining the Halpin Tsai model with the differential quadrature method, they showed that placing more *GPLs* near the outer surfaces increases the natural frequencies and improves stability. Their results also highlighted that higher temperature and axial compression reduce stiffness and enlarge the instability region. Qaderi et al. [7] studied the free vibration of multilayer graphene platelet reinforced composite (*GPLRC*) beams resting on a viscoelastic foundation. Using the Halpin Tsai model and higher-order shear deformation theory with Navier's solution, they examined the influence of *GPL* distribution, foundation parameters, and damping. The results showed that adding *GPLs* and increasing the Pasternak foundation stiffness significantly improve the natural frequencies, while higher damping reduces them. The nonlinear bending behavior of multilayer polymer nanocomposite beams reinforced with graphene platelets (*GPLs*) is investigated by Feng et al. [8]. The analysis is

developed within the framework of Timoshenko beam theory combined with the von Kármán nonlinear strain displacement relation, while the effective properties are estimated using a modified Halpin Tsai model. By employing the Ritz method, the authors conduct a detailed parametric study to assess the effects of *GPL* distribution, geometry, weight fraction, size, and number of layers. The results highlight that even a small amount of *GPLs* can considerably enhance stiffness and reduce deflections, with the most effective reinforcement achieved by dispersing square-shaped *GPLs* near the beam's top and bottom surfaces. Barati and Zenkour [9] examines the post-buckling behavior of porous nanocomposite beams reinforced with graphene platelets (*GPLs*) and sup-ported by a nonlinear hardening foundation. The beam model incorporates shear deformation effects without the need for correction factors, while the material properties are determined using the Halpin Tsai micromechanics model. The authors investigate the combined influences of porosity distribution, *GPL* distribution, weight fraction, geometrical imperfections, and foundation stiffness on the nonlinear buckling response. Results reveal that porosity and *GPL* reinforcement play a decisive role in the stability of both perfect and imperfect beams, with symmetric distributions of porosity and *GPLs* providing the highest post-buckling load capacity. In contrast, uniform porosity weakens structural performance. Moreover, stronger foundation parameters enhance post-buckling resistance, whereas initial imperfections significantly affect the deformation path near critical loading. Mitao et al. [10] analyze the free and forced vibration behavior of functionally graded multilayer graphene platelet (*GPL*)/polymer composite plates using first order shear deformation theory. The material properties are determined through the modified Halpin Tsai model and the rule of mixtures, while the governing equations are solved via a Navier based approach for simply supported plates under dynamic loading. A detailed parametric study highlights the effects of *GPL* distribution, weight fraction, geometry, size, and number of layers on the vibrational performance. Findings show that even a small addition of *GPLs* can significantly enhance natural frequencies and suppress dynamic deflections. The most effective reinforcement is obtained when square-shaped *GPLs* with fewer graphene layers are concentrated near the top and bottom surfaces. Furthermore, adopting a multilayer configuration with about 10–15 layers provides a reliable approximation of the graded profile while maintaining low manufacturing costs. Zhou et al. [11] investigated the free vibratory answer of functional graded porous nanocomposite rectangular plates structure via the general differential quadrature method (*GDQM*) and series solution. The inner porosity and graphene platelets (*GPLs*) are dispersed inside the matrix in three distinct arrangements, either uniformly or non-uniformly. Sobhy et zankour [12] based on shell theory with four variables for shear deformation. An investigation is conducted on the free vibration behavior of composite shallow shells with dual curvature and elastic foundations that are strengthened by functional graded graphene platelets. The Hamiltonian approach is employed to derive the system equations of motion, which are subsequently tackled analytically. Ganapathi et al. [13] utilized higher order trigonometric shear deformation law to examine the dynamic motion behavior of *FG-GPLs* reinforced porous curved beams while taking thickness stretching into account. Mazari et al. [14],[15] have recently conducted complementary studies on the vibrational behavior of graphene platelet reinforced compo-site (*GPLRC*) beams under distinct external fields. In the first study, the vibration of a nanocomposite beam subjected to a uniform thermal effect was analyzed using a semi-analytical Galarkin solution in combination with a linear regression machine learning model. In the second study, the beam was investigated under a non-uniform magnetic field using the same semi-analytical solution method coupled with other machine learning techniques. Together, these works demonstrated that *GPL* distribution patterns, slenderness ratio (*L/H*), and external field intensity play a decisive role in governing the natural frequencies and overall dynamic response of *GPLRC* beams. Piezoelectric components have been widely employed in several essential industrial models and intelligent infrastructures. As a result, they have the ability to transform mechanical energy into electrical energy and vice versa. These special qualities are utilized in many different applications, including sensors, actuators, and power devices [16] and [17]. El Harti et al. [18] investigate the active vibration control of a porous functionally graded (*FGM*) beam operating in a thermal environment using piezoelectric sensors and actuators. The model is developed using the finite element method and Euler Bernoulli beam theory, with the equations of motion derived from Hamilton's principle. Material properties vary through the thickness following a power law, and the study examines the effects of temperature, porosity, and sensor placement. Results show that increasing the power law exponent lowers the natural frequencies due to reduced stiffness, while porosity and temperature amplify vibration amplitudes. Sensor location significantly affects control performance: placing sensors near the free end leads to larger vibration amplitudes and reduces the effectiveness of active control. Zenkour and Aljadani [19] analyze the electro-mechanical buckling of functionally graded piezoelectric plates using a quasi-3D refined plate theory that incorporates thickness stretching effects. The governing equations are derived from the total potential energy principle, and an exact solution is obtained for simply supported rectangular plates with material properties graded through the thickness according to a power law. Results show that including thickness-stretching leads to lower critical buckling loads compared to models that neglect it. Increasing the material exponent reduces stiffness and decreases the buckling load, while the sign and magnitude of applied electric voltage have a strong influence on buckling behavior. The findings provide valuable insights for the design and optimization of *FGP* plate devices under combined mechanical and electrical loading. Alazwari et al. [20] employed the Differential Quadrature Method (DQM) is utilized to examine the crucial buckling temperature of piezoelectric circular Nano plates that are strengthened with evenly dispersed graphene platelets (*GPLs*). The Nano plates are positioned on a flexible substrate and exposed to an external electric field. The results showed that increasing graphene content, elastic foundation stiffness, and electric field enhances buckling resistance, while moisture reduces it. The influence of boundary conditions and nonlocal effects was also highlighted. Qingqing Chen et al. [21] Examine the impact of flexoelectricity upon the vibration behavior of a sandwich Nano beam made of spatially graded porous piezoelectric material and enhanced with graphene platelets (*GPLs*) using the differential quadrature method. This numerical analysis demonstrates that porosity, *GPLs*, and flexoelectricity play a crucial role in governing the vibration behavior of Nano beams. Sobhhy and Mukahal [22] investigated the natural oscillation of piezo electromagnetic plates enhanced by *FG* graphene Nano sheets (*FG-GNSs*) under the influence of outer electric and magnetic potentials. The results show that the fundamental frequency increases with higher graphene content, magnetic potential, and foundation stiffness, while it decreases with larger electric potential, aspect ratio, side to thickness ratio, and power-law index. Mao and Zhang [23] investigated the buckling and post-buckling behavior of a piezoelectric plate strengthened with functionally graded graphene. The plate was subjected to electric

potential and axial pressures. The researchers employed the differential quadrature technique and the first order shear distortion plate theory to analyze the plate's response. Liang et al. [24] developed linear and nonlinear isogeometric finite element models for axially functionally graded graphene platelet reinforced compo-site (*AFG-GPLRC*) curved beams within the framework of third order shear deformation theory and von Kármán's nonlinearity. Using the modified Halpin Tsai model and rule of mixture to predict effective material properties, and solving the governing equations via an isogeometric analysis (*IGA*) approach, they validated their framework against available results. Their parametric study demonstrated the significant influence of geometric parameters, boundary conditions, and *GPL* distribution patterns on the nonlinear bending and vibration responses of *AFG-GPLRC* curved beams. Zhang et al. [25] investigated the nonlinear free vibration and static bending of functionally graded porous graphene platelet reinforced composite plates with integrated piezoelectric patches, incorporating the flexoelectric effect for the first time. Using the Halpin Tsai model, rule of mixture, and *GRF* scheme to evaluate effective material properties, they developed an isogeometric analysis framework based on *FSDT* and von Kármán nonlinearity. Their results highlighted the significant influence of porosity, *GPL* distribution, and weight fraction on the mechanical response, showing that the flexoelectric effect introduces a stiffness hardening mechanism in piezoelectric smart structures. Results show that *GPLs*, especially when concentrated near the surface, significantly improve strength, negative electric voltage enhances stability, and uniaxial loading provides nearly twice the resistance of biaxial loading. No research has yet examined the free vibration behavior of multilayer piezoelectric nanocomposite beams reinforced with functionally graded graphene platelets, under the combined influence of an external electric voltage, a uniform temperature change, and different boundary conditions. This paper addresses this gap by employing a quasi-3D beam theory with stretching effects. The equations of motion are derived using Lagrange's principle and solved through a robust numerical approach specifically, the differential quadrature finite element method (*DQ-FEM*), which integrates the finite element method with the differential quadrature method and has been recently applied in this study [26]. The effects of graphene platelet weight fraction, distribution patterns, length to thickness ratio, and number of layers, external electric voltage, temperature variation, and boundary conditions on the natural frequencies of multilayer functionally graded graphene platelet reinforced nanocomposite beams are systematically investigated.

2. GPLRC BEAM MODEL

In this study, we consider a multilayer piezoelectric nanocomposite beam reinforced with functionally graded graphene platelets, with dimensions L, b, and h.

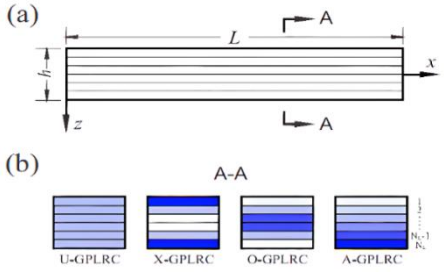

Fig. 1. Dimensions of a GPLRC beam (a), different types of distributions (b)

As seen in Figure 1(a). Throughout the cross sections are defined four different types of reinforcement considered in the current research. The beam has NL layers of uniform thickness for each layer of thickness h/NL, as indicated in Figure 1(b).In the *FG-X* type *GPLRC* beam distribution, the surface layers contain more *GPL*, whereas in the *FG-O GPLRC* type, the mid layers are enriched with *GPLs*. Conversely, in the *FG-A GPLRC* arrangement, *GPL* content steadily rises from the uppermost to the lowermost layer. Notably, in a *UD GPLRC* beam, *GPL* content remains consistent across all layers. Evidently, the *FG-A GPLRC* has asymmetry, but the remaining three distributions display symmetry with respect to the mid-plane [6], [27], [28] and [29].

This study investigates structurally graded *GPLRC* layered beams with an even number of layers. The calculation of the volume fractions v_{GPL} of the k^{th} layer are obtained for each of the four distribution patterns as see in Figure 1 by:

$$U-GPLRC\colon V_{GPL}^{(K)} = V_{GPL}^{*} \tag{1}$$

$$X-GPLRC\colon V_{GPL}^{(K)} = 2V_{GPL}^{*}|2K-N_L-1|/N_L \tag{2}$$

$$O-GPLRC\colon V_{GPL}^{(K)} = 2V_{GPL}^{*}(1-|2K-N_L-1|/N_L) \tag{3}$$

$$A-GPLRC\colon V_{GPL}^{(K)} = 2V_{GPL}^{*}(2K-1)/N_L \tag{4}$$

where *NL* represent is the entire count of layers in the composite beam and k = 1, 2…*NL* is the kth layer. The overall volume fraction of GPLs is determined using:

$$V_{GPL}^{*} = \frac{W_{GPL}}{W_{GPL}+(\rho_{GPL}/\rho_m)(1-W_{GPL})} \tag{5}$$

with

w_{GPL}: the weight fraction of *GPLs*,

ρ_{GPL}: density of graphene platelets,

ρ_m: polymer matrix beam density.

To calculate the appropriate efficient Young's modulus *E* of the beam, the enhanced Halpin-Tsai law is utilized, which considers the impacts and size of *GPL* geometry.

$$E = \frac{3}{8}\frac{1+\zeta_L\eta_L V_{GPL}}{1-\eta_L V_{GPL}} \times E_m + \frac{5}{8}\frac{1+\zeta_T\eta_T V_{GPL}}{1-\eta_T V_{GPL}} \times E_m \tag{6}$$

where

$$\zeta_L = 2(a_{GPL}/b_{GPL}),\ \zeta_T = 2(b_{GPL}/t_{GPL}) \tag{7}$$

$$\eta_L = \frac{(E_{GPL}/E_m)-1}{(E_{GPL}/E_m)+\zeta_L},\ \eta_T = \frac{(E_{GPL}/E_m)-1}{(E_{GPL}/E_m)+\zeta_T} \tag{8}$$

L_{GPL},a_{GPL} and h_{GPL} represent the nominal length, depth, and thickness related to graphene, correspondingly, while E_M and E_{GPL} are the Young's moduli of the piezoelectric matrix and GPLs.

The determination of the following physical parameters, effective linear thermal expansion coefficient *α*, mass density *ρ*, Poisson's ratio *v*, and electrical properties A_{ij}has been done according to the rule of mixtures as:

$$\rho = \rho_{GPL}V_{GPL} + \rho_M V_M \tag{9}$$

$$\upsilon = \upsilon_{GPL}V_{GPL} + \upsilon_M V_M \tag{10}$$

$$\alpha = \alpha_{GPL}V_{GPL} + \alpha_M V_M \tag{11}$$

$$A = A_{GPL}V_{GPL} + A_M V_M \tag{12}$$

In which $V_m + V_{GPL} = 1$ indicates the connection within the volume fractions of the GPL and piezoelectric matrix, V_{GPL} and V_m.

3. EQUATIONS OF MOTION

In which $V_m + V_{GPL} = 1$ indicates the connection within the volume fractions of the *GPL* and piezoelectric matrix, V_{GPL} and V_m. The quasi-3D theory is employed in this study to establish the kinematic relationships of the beam. A key advantage of this theory lies in its ability to account for thickness stretching, which is essential for accurately analyzing thermal vibrations. The displacement expressions associated with the beam's kinematics are given as [30]-[31] and [32]:

$$\begin{aligned} u(x,z,t) &= u_0(x,t) - z\frac{dw_b}{dx} - f(z)\frac{dw_s}{dx} \\ w(x,z,t) &= w_b(x,t) + w_s(x,t) + g(z)w_z(x,t) \end{aligned} \tag{13}$$

Here, u_0 represents the axial displacement of the mid-plane, while the transverse deflection W is decomposed into three components: w_b, w_s, and w_z. The first two components correspond to the bending and shear displacements, whereas w_z *(x)* accounts for the stretching contribution.

The warping function *f(z)* mention in equation (13) is used to describe how both crosswise shear strain and shear stress vary across the thickness of a composite beam.

$$f(z) = \frac{4z^3}{3h^2} \tag{14}$$

$$g(z) = 1 - \frac{df(z)}{dz} \tag{15}$$

Based on the quasi-3D displacement field, strain relations are expressed as follows:

$$\begin{cases} \varepsilon_{11} = \frac{dU}{dx} = \frac{du_0}{dx} - z\frac{d^2w_b}{dx^2} - f(z)\frac{d^2w_s}{dx^2} \\ \varepsilon_{33} = \frac{dW}{dz} = \frac{dg(z)}{dz}w_z(x,t) \\ \varepsilon_{13} = \frac{dU}{dz} + \frac{dW}{dx} = g(z)\left(\frac{dw_s}{dx} + \frac{dw_z}{dx}\right) \end{cases} \tag{16}$$

This is the constitutive relationship for the stresses components, according to the piezo elasticity theory [33]:

$$\begin{Bmatrix} \sigma_{11} \\ \sigma_{33} \\ \sigma_{13} \end{Bmatrix} = \begin{bmatrix} Q_{11} & Q_{13} & 0 \\ Q_{13} & Q_{33} & 0 \\ 0 & 0 & Q_{55} \end{bmatrix} \begin{Bmatrix} \varepsilon_{11} - \alpha T \\ \varepsilon_{33} - \alpha T \\ \varepsilon_{13} \end{Bmatrix} - \begin{bmatrix} 0 & A_{31} \\ 0 & A_{33} \\ A_{15} & 0 \end{bmatrix} \begin{Bmatrix} \hat{E}_1 \\ \hat{E}_3 \end{Bmatrix} \tag{17}$$

By which the Q_{ij} denote the elastic coefficients of the beam that can be stated as:

$$Q_{11} = Q_{33} = \frac{E}{1-\upsilon^2},\ Q_{13} = \frac{E\upsilon}{1-\upsilon^2},\ Q_{55} = \frac{E}{2(1+\upsilon)} \tag{18}$$

In addition, *T* is the applied temperature.

$$T(x,y,z) = T_0 + \Delta T, \tag{19}$$

In which, T_0 represent the ambient room temperature and ΔT is the constant temperature variation.

Moreover, the electric displacements Di have the following writing:

$$\begin{Bmatrix} D_1 \\ D_3 \end{Bmatrix} = \begin{bmatrix} 0 & 0 & A_{15} \\ A_{31} & A_{33} & 0 \end{bmatrix} \begin{Bmatrix} \varepsilon_{11} - \alpha T \\ \varepsilon_{33} - \alpha T \\ \varepsilon_{13} \end{Bmatrix} + \begin{bmatrix} s_{11} & 0 \\ 0 & s_{33} \end{bmatrix} \begin{Bmatrix} \hat{E}_1 \\ \hat{E}_3 \end{Bmatrix} \tag{20}$$

The relationship of the electric field is:

$$\begin{Bmatrix} \hat{E}_1 \\ \hat{E}_3 \end{Bmatrix} = \begin{Bmatrix} \frac{d\psi}{dx}cos\left(\frac{\pi z}{h}\right) \\ -\frac{\pi}{h}\psi sin\left(\frac{\pi z}{h}\right) \end{Bmatrix} - \begin{Bmatrix} 0 \\ \frac{2\bar{V}_0}{h} \end{Bmatrix} \tag{21}$$

Whereas ψ is the intermediate surface electric potential of the beam and V_0 is the external electric voltage.

$$\bar{V}_0 = V_0 h^2 E_{GPL} \tag{22}$$

4. EQUATIONS OF MOTION DERIVATION

The motion equations can be extracted from Lagrange's principle in the next form:

$$\frac{d}{dt}\left(\frac{\partial L}{\partial \dot{q}_i}\right) + \frac{\partial L}{\partial q_i} = 0 \tag{23}$$

Where q_i are the unknown coefficients u_0, w_b, w_s et w_z. $\dot{q}$ is the time derivative of q and L is the total energy, which includes strain, kinetic and Strain energies [26],[30],[32],[33],[34],[35] and [36].

Where the strain energy is written as follow:

$$U_b = \frac{1}{2}\int \left(\sigma_{ij}\varepsilon_{ij} - D_i E_i\right) dv \tag{24}$$

By substituting Eqs. (16), (17), (20), and (21) into Eq. (24), the final formulation of the strain energy is obtained as presented in Appendex A (see Eqs. (A.1)– (A.3)).

The defined kinetic energy $K_b$related to studied problem is provided by next formula:

$$K_b = \frac{1}{2}\int \rho\left(\dot{U}^2 + \dot{V}^2 + \dot{W}^2\right)\, dv \tag{25}$$

The following formula is obtained by deriving the displacement field and replacing it in the earlier equation.

$$K_b = \frac{1}{2}\int \rho\left(\left(\dot{u}(x,t) - z\frac{d\dot{w}_b}{dx} - f(z)\frac{d\dot{w}_s}{dx}\right)^2 + (\dot{w}_b(x,t) + \dot{w}_s(x,t) + g(z)\dot{w}_z(x,t))^2\right)\, dv \tag{26}$$

$$K_b = \frac{1}{2}\int_0^l \begin{pmatrix} J_1(\dot{u}^2 + \dot{w}_b^2 + \dot{w}_s^2 + 2\dot{w}_b\dot{w}_s) \\ -2J_2\dot{u}\frac{d\dot{w}_b}{dx} - 2J_3\dot{u}\frac{d\dot{w}_s}{dx} \\ +2J_4\frac{d\dot{w}_b}{dx}\frac{d\dot{w}_s}{dx} + J_5\left(\frac{d\dot{w}_b}{dx}\right)^2 \\ +J_6\left(\frac{d\dot{w}_s}{dx}\right)^2 + J_7\dot{w}_z^2 \\ +2J_8(\dot{w}_b\dot{w}_z + \dot{w}_s\dot{w}_z) \end{pmatrix} dx \tag{27}$$

where

$$\{J_1 : J_8\} = b\rho\int_{-\frac{h}{2}}^{\frac{h}{2}}(1, z, f, zf, z^2, f^2, g^2, g)dz \tag{28}$$

Using Eq. (29), the potential energy V_b of the multilayer *FG-GPLRC* beam in response to an applied externally applied electric voltage and a constant temperature variation is described [6]:

$$V_b = -\frac{1}{2}\int_0^l N_{TOT}\left(\frac{dW}{dx}\right)^2 dx \tag{29}$$

with

$$\begin{aligned} \left(\frac{dW}{dx}\right)^2 &= \left(\frac{dw_b}{dx}\right)^2 + \left(\frac{dw_s}{dx}\right)^2 + 2\frac{dw_b}{dx}\frac{dw_s}{dx} \\ &+ g^2\left(\frac{dw_z}{dx}\right)^2 + 2g\frac{dw_b}{dx}\frac{dw_z}{dx} + 2g\frac{dw_s}{dx}\frac{dw_z}{dx} \end{aligned} \tag{30}$$

Equation (31) is the result of substituting Equations (29)–(30):

$$V_b = -\frac{1}{2}\int_0^l N_{TOT}\begin{pmatrix}\left(\frac{dw_b}{dx}\right)^2+\left(\frac{dw_s}{dx}\right)^2\\ +2\frac{dw_b}{dx}\frac{dw_s}{dx}+g^2\left(\frac{dw_z}{dx}\right)^2\\ +2g\frac{dw_b}{dx}\frac{dw_z}{dx}\\ +2g\frac{dw_s}{dx}\frac{dw_z}{dx}\end{pmatrix}dx \quad (31)$$

5. THE COUPLED DIFFERENTIAL QUADRATURE FINITE ELEMENT METHOD

5.1. The improved differential quadrature rule

Differential quadrature technique is numerical method that estimate the derivatives of a given function by calculating a weighted sum of field variables along a line that passes through a certain point. The test functions for polynomial basis functions *DQM* are implemented using a collection of Lagrange polynomials [[26]26,37].

Hence, the derivative of the subject function *f(x)* of degree n at a discrete position x_i may be expressed as:

$$\frac{\partial^n f(x;t)}{\partial x^n} = \sum_{j=1}^{N} A_{ij}^{(n)} f(x_j;t) \quad (i = 1,2,3,\ldots,N) \quad (32)$$

The weighting coefficient, denoted as $A_{ij}^{(n)}$, is a parameter related to the order n derivative. When n is equal to 1, the weighting factor will be determined in the following manner.

$$\begin{aligned} A_{ij}^{(1)} &= \frac{M(x_i)}{(x_i-x_j)M(x_j)} \quad i \neq j, j = 1,2,\ldots,N \\ A_{ii}^{(1)} &= -\sum_{j=1,j\neq i}^{N} A_{ij}^{(1)} \quad i = 1,2,\ldots,N \end{aligned} \quad (33)$$

where

$$\begin{aligned} M(x_i) &= \prod_{k=1,k\neq i}^{N}(x_i - x_k) \\ M(x_j) &= \prod_{k=1,k\neq i}^{N}(x_j - x_k) \end{aligned} \quad (34)$$

The given recurrence connection is utilized to compute the weighting factors for second and larger-order derivatives. If n > 1, which is given as:

$$\begin{aligned} A_{ij}^{(n)} &= n\left(A_{ij}^{(1)} * A_{ii}^{(n-1)} - \frac{A_{ij}^{(n-1)}}{(x_i-x_j)}\right) \\ & i \neq j, i, j = 1,2,\ldots,N, n > 1 \\ A_{ii}^{(1)} &= -\sum_{j=1,j\neq i}^{N} A_{ij}^{(1)} \quad i = 1,2,\ldots,N \end{aligned} \quad (35)$$

5.2. Gauss-Lobatto quadrature principle

Gauss-Lobatto quadrature rules refer to a mathematical topic is available in various works of mathematics. The quadrature rule of Gauss Lobatto for a given function f(x) as prescribed in [-1, 1] with a degree of accuracy (2n-3) is as follows [26]:

$$\int_{-1}^{1} f(x)dx = \sum_{j=1}^{N} C_j f(x_j) \quad (36)$$

Integration can be obtained using the Gauss-Lobatto weighting coefficient $C_j$as follows:

$$C_1 = C_N = \frac{2}{N(N-1)},$$

$$C_j = \frac{2}{N(N-1)[P_{N-1}(x_j)]^2} \quad (j \neq 1, N) \quad (37)$$

The (*j*-1) root of the primary derivative of $P_{N-1}(x)$ is denoted by x_j. Equations (38) and (39) of the recursively formula will be used to solve the Legendre polynomials' roots. This will facilitate the process of locating numerous roots.

$$P_{N+1}(x) = \frac{2N+1}{N+1}xP_N(x) - \frac{N}{N+1}P_{N+1}(x) \quad (38)$$

By which$P_0(x) = 1$, $P_1(x) = x$. The following formula can be used to find the n^{th} order derivation of the Legendre polynomials:

$$P_{N+1}^{(n)}(x) = xP_N^{(n)}(x) + (N+n)P_N^{(n)}(x) \quad (39)$$

The selection of sampling points depends on the grid distribution of Gauss-Lobatto nodes to offer a higher density of points near the boundaries.

$$x_j = -cos\left(\frac{j-1}{N-1}\pi\right) \quad (40)$$

Iteratively solving Gauss-Lobatto nodes is done using the Newton-Raphson technique.

$$x^{iT+1} = x^{iT} - F'^{(x^{iT})^{-1}}F(x^{iT}), \quad iT = 0,1,\ldots \quad (41)$$

in which

$$x = [x_2, x_3, \ldots, x_{N-1}]^T$$

$$x = [x_2, x_3, \ldots, x_{N-1}]^T \quad (42)$$

$$F(x) = [f(x_2), f(x_3), \ldots, f(x_{N-1})]^T \quad (43)$$

$$F'(x) = \left[\frac{\partial f(x_j)}{\partial x_i}\right]_{(N-2)\times(N-2)} \quad (44)$$

$$f(x_j) = \sum_{k=1,k\neq j}^{N} \frac{1}{x_j - x_k} \quad j = 2,3,\ldots,N-1 \quad (45)$$

$$\frac{\partial f(x_j)}{\partial x_i} = \begin{cases} -\sum_{k=1,k\neq j}^{N} \frac{1}{(x_j-x_k)^2}, & (i = j) \\ \frac{1}{(x_j-x_k)^2}, & (i \neq j) \end{cases} \quad (46)$$

In the i^{th}iteration step, *k* represents the value of *x*. This approach exhibits less sensitivity to the beginning value. Equation (46) provides the numerical estimations that are utilized like initial values.

5.3. The enhanced Finite element method based Differential Quadrature

A variety of engineering problems can be solved numerically with the help of the finite element method (*FEM*), which is recognized as an efficient numerical tool.

Unfortunately, there are instances when this approach struggles with numerical instability, speed of computation, and convergence. To improve its robustness, stability, and speed in the calculus, this method must now be combined with other numerical or semi-numerical methods. With the purpose to parametrize the system energies, "the differential quadrature "rules and Gauss-Lobatto quadrature are applied [26].

Considering that the function of deflection is:

$$u(x) = \sum_{i=1}^{N} L_i(x) u_i$$
$$w(x) = \sum_{i=1}^{N} L_i(x) w_i \quad (47)$$

Where the Lagrange polynomial is represented by L_i, the motions of the Gauss Lobatto quadrature nodes or the *DQ* nodal shifts of the beam finite element are represented by u_i and w_i.The formulas for strain, kinetic and potential energies in equations (A.1-27-31) may be expressed are presented in Appendix A as Eqs. ((A.4)–(A.6)), using Gauss-Lobatto quadrature and *DQ* rules.

Equations (33–35) are used in order to compute the matrices containing the weighting factors for the *DQ* procedures for the initial and second order derivatives, correspondingly, by respect to the Gauss Lobatto nodes. These matrices are shown by $A^{(1)}$ and $A^{(2)}$.

$$C = diag[C_1, C_2, \ldots C_N] \quad (48)$$

Where C_j represent the corresponding weighting factors of integration by Gauss-Lobatto.

$$\bar{u}^T = [u_1 u_2 \ldots u_N]$$
$$\bar{w}^T = [w_1 w_2 \ldots w_N] \quad (49)$$

To achieve coherence within elements, the element motion vectors must be constructed:

$$u^T = [u_1 u_3' u_3 \ldots u_{N-2} u_N u_N']$$
$$w^T = [w_1 w_3' w_3 \ldots w_{N-2} w_N w_N'] \quad (50)$$

The relationship between u and w is established by the utilization of the *DQ* rule:

$$u = Q\bar{u}, \quad w = Q\bar{w} \quad (51)$$

with

$$Q = \begin{bmatrix} 1 & 0 & 0 & \cdots & 0 & 0 \\ A_{1,1}^{(1)} & A_{1,2}^{(1)} & A_{1,3}^{(1)} & \cdots & A_{1,N-1}^{(1)} & A_{1,N}^{(1)} \\ 0 & 0 & 1 & \cdots & 0 & 0 \\ \vdots & \vdots & \vdots & \ddots & \vdots & \vdots \\ 0 & 0 & 0 & \cdots & 0 & 1 \\ A_{N,1}^{(1)} & A_{N,2}^{(1)} & A_{N,3}^{(1)} & \cdots & A_{N,N-1}^{(1)} & A_{N,N}^{(1)} \end{bmatrix} \quad (52)$$

For quadrature and differentiation, all node distribution types are [-1, 1]. Thus, to utilize them in practical applications, it is necessary to make the following modifications to the differential and quadrature matrices:

$$\bar{C} = \frac{l_e}{2} C, \quad \bar{A}^{(1)} = \frac{2}{l_e} A^{(1)}, \quad \bar{A}^{(2)} = \frac{4}{{l_e}^2} A^{(2)} \quad (53)$$

By which the length of the beam element is written by l_e.

It is possible to replace the energy using Eqs. (32)–(52). To derive the fundamental equations of motion, Eqs. (A.1), (27), and (31) are combined to obtain Eq. (A.7), where the constituents of the mass and stiffness matrices are presented in Appendix as Eqs. (A.8) and (A.9), respectively.

6. NULERICAL RESULTS

This section presents the comprehensive quantitative findings for the dynamic examination of a piezoelectric beam reinforceded with functionally graded graphene platelets that was exposed to an external electric voltage in a thermal environment considering several ends supports, including clamped- clamped *(CC)*, simply supported- simply supported *(SS)*, clamped-free *(CF)*, and clamped-simply supported *(CS)*. Unless specified otherwise, the simply supported-simply supported *(S-S)* beam and the following constant data were used in the numerical examples:

$L_{GPL} = 2.5\ \mu\text{m}, b_{GPL} 1.5\ \mu\text{m}, h_{GPL} = 1.5\ \text{nm}, \frac{L}{h} = 5, W_{GPL} = 0.5\%, L = 1\text{m}, NL = 20, e_0 = 1000$.

The non-dimensional natural frequency indicated below is used for all findings in tables and figures.

$$\bar{\omega} = \omega h \sqrt{\frac{\rho_m}{E_m}} \quad (54)$$

The piezoelectric matrix and *GPL* properties are presented in Table 1 as [21] and [32].

Tab. 1. Material constituents and properties

Materials	Piezoelectric	GPLs
E(Gpa)	1.4	1010
$\boldsymbol{\nu}$	0.29	0.186
$\boldsymbol{\rho(g/cm^3)}$	1.92	1.06
$\boldsymbol{\alpha(10^{-6}K^{-1})}$	60	5
$\mathbf{A_{31}(10^{-3}C/m^2)}$	50.535	50.535 e_0
$\mathbf{A_{33}(10^{-3}C/m^2)}$	13.212	13.212 e_0
$\mathbf{A_{15}(10^{-3}C/m^2)}$	-15.93	-15.93 e_0
$\mathbf{s_{11}(10^{-9}C/Vm)}$	0.5385	0.5385 e_0
$\mathbf{s_{33}(10^{-9}C/Vm)}$	0.59571	0.59571 e_0

6.1. Convergence investigation

To investigate the convergence of the current assessment, Table 2 lists the non-dimensional basic frequencies of *S-S* multilayer *GPL*/piezoelectric nanocomposite beams with various reinforcing forms, such as "*UD*, *FG-O*, *FG-X*, and *FG-A*". This study considers varying numbers of elements and grid points, with a fixed number of layers *NL=20*, *L/h=5* and a weight fraction W_{GPL}=0,5%. In Figure 2, the number of elements is fixed at $N_e = 1$ while the number of grid points is varied. Conversely, in Figure 3, the number of grid points is fixed at *N*=6 while the number of elements is changed.

Tab. 2. Convergence study of *DQFEM* related to linear free vibration nanocomposite beam armed with *GPLs*

Ne	*N*	*UD*	FG-*X*	FG-*O*	FG-A
1	4	0.3061	0.3637	0.2351	0.3062
	6	0.2742	0.3258	0.2105	0.2674
	8	0.2741	0.3257	0.2104	0.2673
	10	0.2741	0.3257	0.2104	0.2673
2	4	0.2752	0.3270	0.2113	0.2686
	6	0.2741	0.3257	0.2104	0.2673
	8	0.2741	0.3257	0.2104	0.2673
	10	0.2741	0.3257	0.2104	0.2673
3	4	0.2743	0.3259	0.2106	0.2676
	6	0.2741	0.3257	0.2104	0.2673
	8	0.2741	0.3257	0.2104	0.2673
	10	0.2741	0.3257	0.2104	0.2673

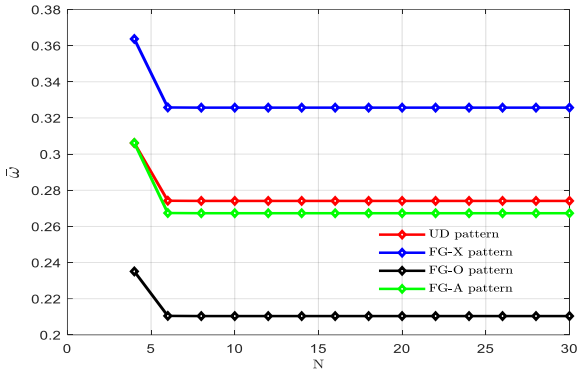

Fig. 2. Convergent of the vibration frequency of a piezoelectric beam armed with *GPLs* as a function of the amount of grid points

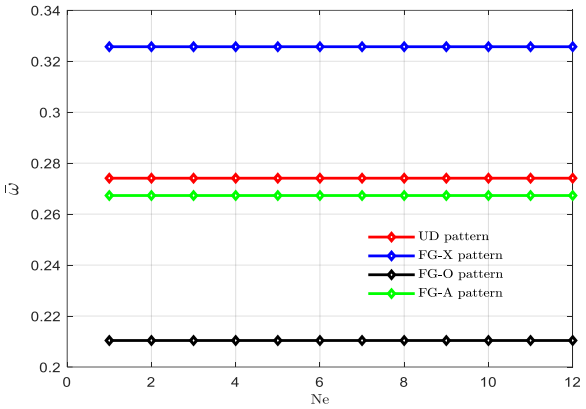

Fig. 3. The convergence of the natural frequency of a piezoelectric beam reinforced with graphene platelets as a variable dependent on the quantity of components

As observed in Figures 2 and 3, the outcomes begin to converge at *N=4* with *Ne=1*, and achieve full convergence at *N=6* with *Ne=1*. These results confirm the efficiency of the proposed method in delivering highly accurate solutions with minimal computational increments. In addition, the convergence behavior is not affected by the type of graphene platelet distribution, which mainly influences the values of the non-dimensional natural frequency. Specifically, the *FG-X* distribution yields the highest natural frequency, followed by the *UD* and *FG-A* distributions, while the *FG-O* distribution exhibits the lowest values. Based on these observations and to ensure consistency with previous studies in the literature, we adopt *N=10* sample points and *Ne=1* element for the remainder of the research.

6.2. Comparison studies

To verify the coherence and precision of the current findings from the novel resolution procedure based DQ-FEM for different boundary conditions, the non-dimensional natural frequency of an FG beam is checked with those given by Şimşek et al.[38] beam model in Table 3, for numerous L/h proportion, and k=0.3 is used as the power law exponent. The properties that follow related to the ceramic (Alumina) and metal (Aluminum) used to make the FG beam:

Alumina: $E_c = 380\ Gpa, \rho_c = 3800\ kg/m^3, v_{\mathrm{m}} = 0.23$

Aluminum: $E_m = 70\ Gpa, \rho_m 2700 kgm^3, v_{\mathrm{m}} = 0.23$

The following formula is used to represent the non-dimensional vibration frequency for validation purposes.

$$\bar{\omega} = \omega L^2 \sqrt{\frac{I_1}{h^2 \int_{-h/2}^{h/2} E\, dz}}, \quad I_1 = \int_{-h/2}^{h/2} \rho\, dz \tag{55}$$

Table 3 shows that for different *L/h* ratios (10, 30, and 100) and numerous end supports, the present results are in good agreement with the reference solutions reported by Şimşek [37].

Tab. 3. Comparative examination of the natural frequencies of various boundary conditions with varying *L/h* ratios

BC		*L/h*=10	*L/h*=30	*L/h*=100
S-S	Şimşek [37]	2.695	2.737	2.742
	Present	2.739	2.775	2.779
C-F	Şimşek [37]	0.969	0.976	0.977
	Present	0.976	0.982	0.983
C-C	Şimşek [37]	5.811	6.167	6.212
	Present	5.947	6.242	6.279

Tab. 4. Comparative of non-dimensional frequency with Wu et al. 7 for various *GPL* distributions at ΔT = 0 *K*, *L/H* = 10, and W_{GPL}= 0.3%

	Pure epoxy	UD	FG-X	FG-O	FG-A
Wu et al.[6]	0.5998	0.8475	0.9293	0.7508	0.8164
Present	0.5977	0.8445	0.9300	0.7401	0.8158

For the second comparison, Table 4 presents the non-dimensional frequencies of *FG* multilayer graphene platelet–reinforced composite beams with different *GPL* distribution patterns, considering a weight fraction of 0.3% and an aspect ratio of *L/h*=10, under clamped–clamped (*C–C*) boundary conditions. The material properties are taken as follows: $E_m = 3\ Gpa,\ \rho_m = 1200 kg/m^3$, $\boldsymbol{\nu}_m = 0.3$ and $\alpha_m = 60 \times 10^{-6} K^{-1}$ for the polymer matrix and $E_{GPL} = 1010\ Gpa,\ \rho_{GPL} = 1062.5\ kg/m^3,\ \boldsymbol{\nu}_{GPL} = 0.186$ and $\alpha_{GPL} = 5 \times 10^{-6} K^{-1}$ for Graphene Platelets. The results show that, across all *GPL* distribution patterns, the present model is in close agreement with the reference solution.

Additionally, Table 5 reports a validation of the present *DQ-FEM* formulation under thermal effects by comparing the fundamental frequency of a *C–C FG-X* beam (*L/h*=10, $W_{GPL} = 0.3\%$) with the reference data provided by Wu et al. [6] for (ΔT=0,50, and 100*K*). The close agreement confirms the accuracy and reliability of the proposed method.

Tab. 5. Comparative of the non-dimensional fundamental frequency ω_1 for *Ps/Pcr*=0 between the present results and those of Wu et al. under different temperature conditions

ΔT	Present	Wu et al.[6]
0 K	0.9666	0.9289
50 K	0.9275	0.8883
100 K	0.8865	0.8501

The non-dimensional frequency can be represented by the following formula:

$$\bar{\omega} = \omega L \sqrt{\frac{I_{00}}{A_{110}}}, \quad I_{00} = \int_{-\frac{h}{2}}^{h/2} \rho_m \, dz,$$

$$A_{110} = \int_{-h/2}^{h/2} Q_{11} \, dz \tag{56}$$

6.3. Parametric examination

Figure 4 displays the non-dimensional frequency for *S-S* (simply supported-simply supported) *GPLRC* beam with varying numbers of layers, $W_{GPL} = 0.5\%$ and *L/h=5*. It is observed that for *UD* and *FG-A* distributions, the frequency remains nearly unchanged as the number of layers increases, whereas it increases for *FG-X* and decreases for *FG-O*. Moreover, the results stabilize when the number of layers reaches *NL=15*. Consequently, *NL=20* will be used to acquire all research findings, ensuring maximum accuracy. Among the four distribution patterns, the beam with *UD* pattern is the least affected by variations in *NL*.

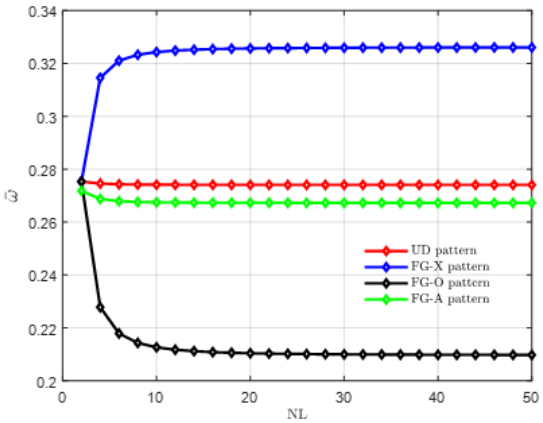

Fig. 4. The no-dimensional frequency in relation to the quantity of layers (*NL*) with respect to various forms

The linear vibration frequency result of simply support- simply support *FG* piezoelectric reinforced beam considering various *GPLs* weight fraction, different patterns and a wide range of length-to-depth ratios (*L/h*) is showed in Table 6. We can clearly see from the obtained outcomes, that the weight fraction and length to thickness ratio have significant impacts on frequency parameter. The behavior by vibration frequency increases as the weight fraction increases. Conversely, As the *L/h* ratio grows, the natural frequency decreases. The beam with *FG-X* reinforcement offers the extreme natural frequency, tracked by UD, *FG-A*, and *FG-O* types reinforcements. This is because, compared to other distributions, the composite beam with the *FG-X* pattern exhibits significantly higher rigidity.

Tab. 6. Dynamic results of *FG-GPLRC* piezoelectric beam diverse types of distribution and different values of the length-to-thikness proportion *L/h*

W_{GPL}	Patterns	UD	FG-X	FG-O	FG-A
0.1%	L/h=5	0.1581	0.1765	0.1373	0.1569
	L/h =10	0.0448	0.0448	0.0348	0.0398
	L/h 15	0.0179	0.0200	0.0155	0.0177
	L/h =20	0.0101	0.0112	0.0087	0.0100
0.3%	L/h=5	0.2237	0.2618	0.1776	0.2194
	L/h =10	0.0567	0.0665	0.0450	0.0557
	L/h 15	0.0253	0.0296	0.0201	0.0248
	L/h =20	0.0142	0.0167	0.0113	0.0140
0.5%	L/h=5	0.2741	0.3257	0.2104	0.2673
	L/h =10	0.0695	0.0827	0.0533	0.0678
	L/h 15	0.0310	0.0368	0.0238	0.0302
	L/h =20	0.0174	0.0207	0.0134	0.0170

Tab. 7. Dynamic Change in the non-dimensional frequency of the *S-S* beams for different temperatures changes, different patterns and various values for weight fraction

ΔT	W_{GPL}	0.1%	0.3%	0.5%
0	UD	0.1581	0.2237	0.2741
	FG-X	0.1765	0.2618	0.3257
	FG-O	0.1373	0.1776	0.2104
	FG-A	0.1569	0.2194	0.2673
100	UD	0.1413	0.2000	0.2451
	FG-X	0.1616	0.2419	0.3017
	FG-O	0.1175	0.1467	0.1711
	FG-A	0.1415	0.1983	0.2417
200	UD	0.1221	0.1730	0.2122
	FG-X	0.1452	0.2201	0.2757
	FG-O	0.0936	0.1071	0.1194
	FG-A	0.1240	0.1741	0.2122

Table 7 exhibits the temperature change impacts with weight fraction on the first natural frequency of piezoelectric *GPLRC* beam for various distributions ("*FG-X*, *UD*, *FG-O*, and *FG-A*"). The outcomes indicate that an increase in temperature changes ΔT (0, 100, and 200) resulted in a decrease in non-dimensionless frequencies. As well as, the non-dimensionless frequencies decrease for all distributions when "the length of the beam to thickness *(L/h)*" ratio increases, indicating that these characteristics may have a considerable influence on the frequency. Additionally, similar to other former results, *FG-X* provides the highest frequency, while *FG-O* gives the lowest. *UD* and *FG-A* rank just after *FG-X* pattern respectively for all *L/h* values.

Figure 5 shows that the natural frequency decreases as *L/h* increases, with the *FG-X* distribution giving the highest values. Under a thermal load (ΔT=100*K*), the frequencies drop further because thermal stresses reduce the beam's stiffness. When *L/h*>10, the trend becomes irregular. This happens because slender beams have very low flexural rigidity, and thermal compressive stresses weaken them even more. As a result, the beam becomes highly sensitive to small disturbances, which explains the instability observed in the frequency response.

Figure 6 illustrates the impact of the weight fraction and dispersion forms of *GPL* on the non-dimensional frequency of *FG* graphene composite beams. It is observed that the frequency increases even with a little dose of *GPL*, and that this enhancement increases with more GPL weight fractions. In addition, compared with the "*UD, FG-O* and *FG-A GPLRC* beams, the *FG-X GPLRC* beam" can vibrate in higher values of frequency.

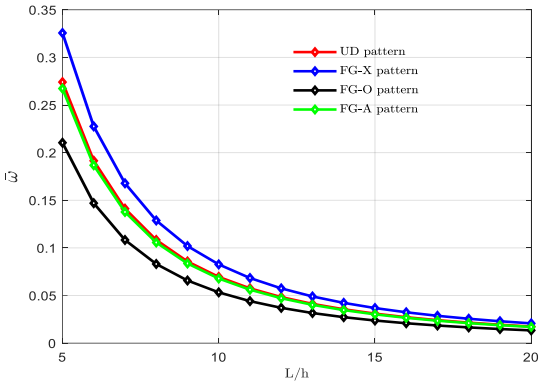

(a)

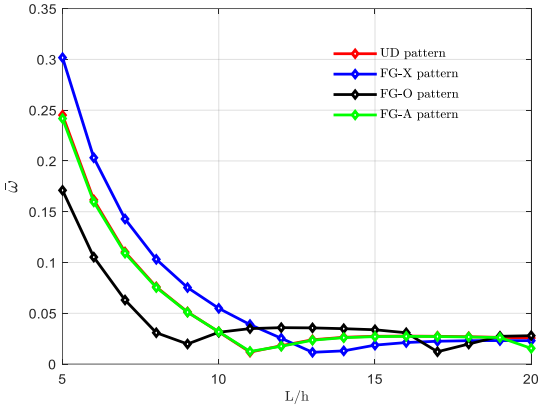

(b)

Fig. 5. The no-dimensional The impact of the beam's span-to-thickness portion on the natural frequency of *GPLRC* beams (a) $\Delta \boldsymbol{T} = \boldsymbol{0K}$ and (b) $\Delta \boldsymbol{T} = \boldsymbol{100K}$

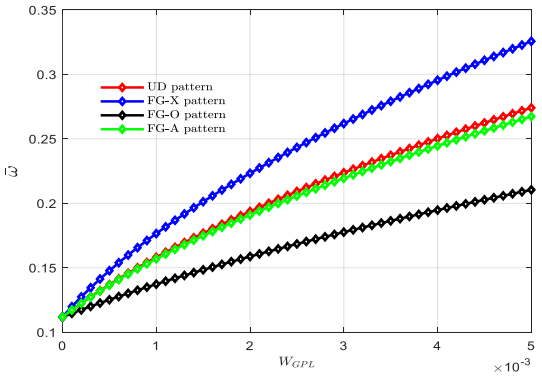

(a)

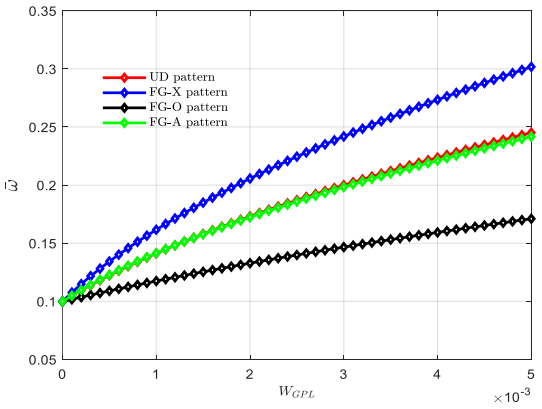

(b)

Fig. 6. The impact of the L/h portion on the no dimensionless natural frequency related to *GPLRC* beams (a) $\Delta \boldsymbol{T} = \boldsymbol{0K}$ and (b) $\Delta \boldsymbol{T} = \boldsymbol{100K}$

Figure 7 illustrates the effect of *GPLs* geometric and dimension on the ultimate vibratory frequency parameter of *GPLRC* beam with *FG-X*. A greater ratio of a_{GPL}/b_{GPL} denotes a bigger *GPL* surface area; whereas a greater number of b_{GPL}/t_{GPL} indicate that, every single *GPL* has a reduced number of graphene layers. This figure's outcomes shows that an increase in $\mathrm{a_{GPL}/b_{GPL}}$ and b_{GPL}/t_{GPL} causes the non-dimensionless frequency to rise for all numerical values of ΔT. $\mathrm{a_{GPL}/b_{GPL}}$ and $\mathrm{b_{GPL}/t_{GPL}}$ effects become considerably less noticeable when b_{GPL}/t_{GPL} is greater than 10^3 and the frequency seems to stabilize. In addition, Figures 5, 6 and 7 make it clear that as the temperature disparity (ΔT) expand, the value of vibratory frequency reduce, indicating a drop in the global stiffness of the structure.

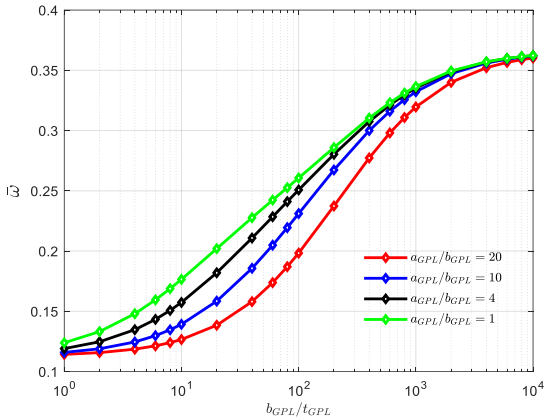

(a)

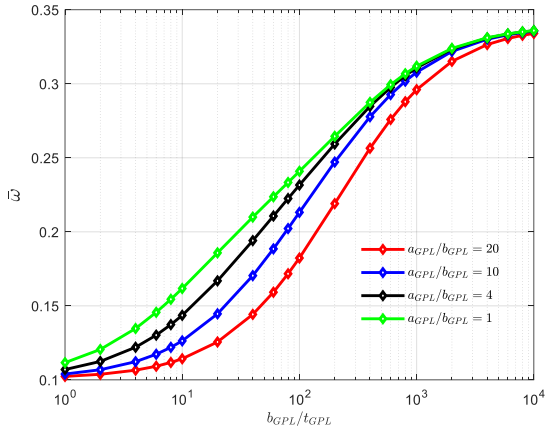

(b)

Fig. 7. The impact of GPL dimensions and geometry on the vibratory frequency of FG-X type GPRLC beam (a) $\Delta \boldsymbol{T} = \boldsymbol{0K}$ and (b) $\Delta \boldsymbol{T} = \boldsymbol{100}$

For a multi-layer "*FG-X GPLRC*" beam, considering *L/h=5*, $W_{GPL} = 0.5$ and simply supported boundary conditions on both sides, Figure 8 shows the effect of the weight fraction and temperature change on the non-dimensionless frequency. Due to the high thermal conductivity of graphene, the results indicate a decrease in frequency as the temperature difference increases. This effect becomes more pronounced at higher *GPL* weight fractions.

The variations in the non-dimensional vibratory frequency of *FG-X* pattern taking into consideration diverse values of the voltage V_0 applied from an external source against the weight fraction W_{GPL}, and considering numerous values of piezoelectric factor e_0 in the corresponding figures a ($e_0 = 100$), b ($e_0 = 300$), c ($e_0 = 600$) and d ($e_0 = 1000$) are illustrated in Figure 9. As noted, that

the beam stiffness decreases as the external electric voltage V_0 increases leading to a decrement in the natural frequency. It is apparent, from all the figures that the impact of V_0 on natural frequency becomes more significant as the weight fraction and the piezoelectric multiple increases, due to the high electrical conductivity of the graphene platelets.

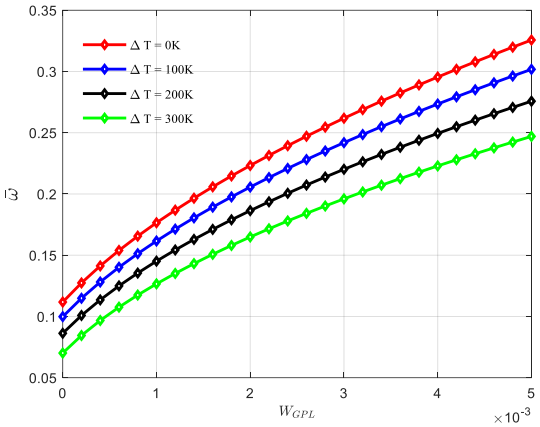

Fig. 8. The impact of the weight portion and temperature increase on the no dimensional vibration frequency of *GPLRC* beams

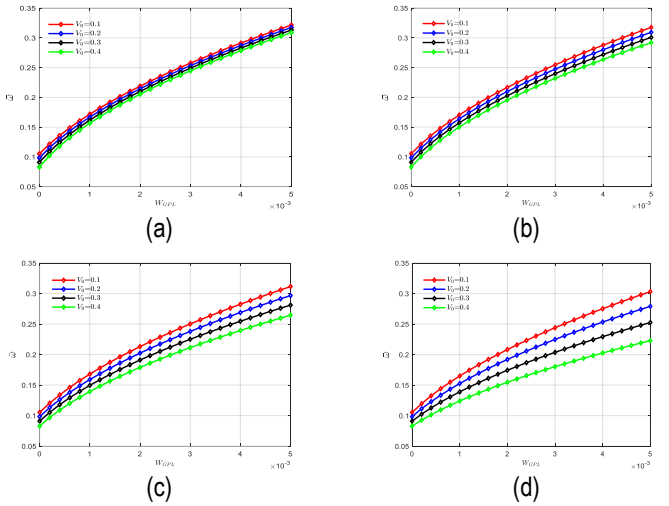

Fig. 9. The influence of the external electric voltage and piezoelectric component on the vibration frequency of *FG-GPLRC* beams

In Figure 10, a three dimensional bar chart depicting the change in the value of natural frequency related to a simply supported simply supported reinforced *GPL* beams is shown. This representation considers different values of external electric voltage and temperature difference, with an *FG-X* dispersion pattern. It is observed that the frequency steadily decreases as the temperature difference diminishes and electric voltage parameters increase, this is in line with the well-established idea that higher values of these parameters weaken structural rigidity.

The influence of diverse end supports on the non-dimensional frequency for an *FG-X* pattern with *L/h*=5 and different weight fraction values are displayed in Figure 11. As can be observed, the clamped-clamped boundary condition yields the highest vibration frequency, followed by the clamped-simply supported and simply supported-simply supported configurations. In contrast, the clamped-free boundary condition results in the lowest natural frequency values.

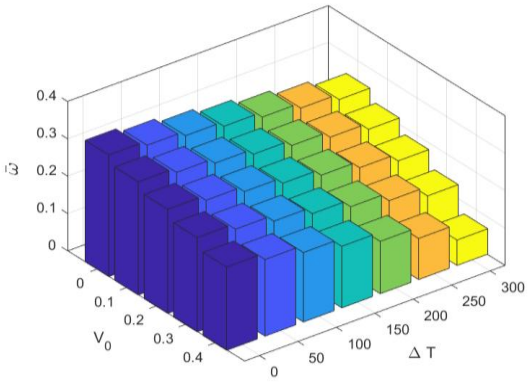

Fig. 10. Natural Frequencies as Three-Dimensional Bar Chart Under different values of External Electric Voltages and Temperature Differences values

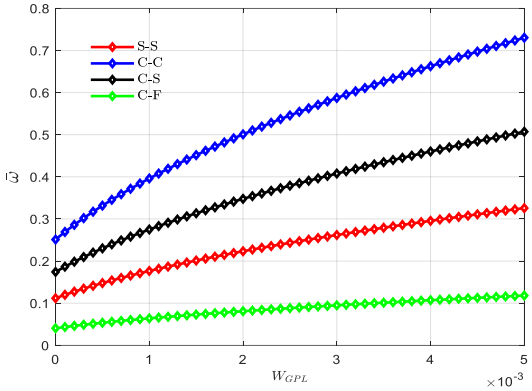

Fig. 10. Impact of boundary conditions on the natural frequency of *GPLRC* beams

Table 8 exhibits the numerical values for the free variation in the non-dimensional frequency of reinforced nanocomposite beams by layered *GPLs* in *FG-X* repartition with W_{GPL}=0.5% for various *L/h* values and boundary conditions. As expected, a considerably higher natural frequency is seen for the *C-C* beam type support for all *L/h* ratio values followed by *C-S*, *S-S* and finally *C-F* nanocomposite beam. In addition, as seen an increment the slenderness ratios lead to the reduction in the ultimate results by the vibratory response of the nanocomposite beam as a result of the decrease in the pliability of the composite structure.

Tab. 8. Frequency values of functionally graded multilayer *X-GPLRC* beams with varying boundary conditions and slenderness ratios

BC	L/h=5	L/h=10	*L/h=15*	L/h=20
S-S	0.3257	0.0827	0.0368	0.0207
C-C	0.7302	0.1888	0.0844	0.0476
C-S	0.5071	0.1297	0.0579	0.0326
C-F	0.1180	0.0297	0.0132	0.0074

7. CONCLUSION

In This Work. The study investigates the free vibration characteristics of multilayered piezoelectric beams reinforced with functionally graded graphene platelets (*FG-GPLRC*). The beams are

subjected to an external electric voltage and uniform temperature variation, considering various boundary conditions. The effective Young's moduli have been derived for the beam under the Halpin-Tsai model. The Poisson's ration, "mass density", thermal expansion coefficient, and piezoelectric characteristics were derived under four different *FG-GPL* distribution types of the ruling mixture. The displacement components were represented using an improved shear and stretched deformation beam approach. (*Q3DBT*) concerning the effect of stretching thickness. Moreover, the equations of motion were obtained by Lagrange's principle. In addition, these formulations were verified through comparative analysis with results from other previous publications. According to the results of this investigation, some crucial conclusions can be drawn as follows:

- The employed *DQFEM* based numerical tool has a fast convergence, compact computation execution time machine, and robust numerical stability, where it converges for one element and a number of sampling points equal to 6.
- When comparing the current *DQFEM* to the traditional finite element approach and analytical solutions, and the computation times are notably faster.
- For all possible forms of *FG-GPL* distribution, it was determined that when we increase in "the external electric voltage, the piezoelectric" factor and the applied temperature results in a reduction in structural stiffness. The impacts of external electric voltage and temperature difference on natural frequency becomes more significant as the weight fraction and the piezoelectric multiple increases, Because of the graphene platelets' excellent thermal and electrical conductivity.
- The type of distribution of the *GPL* has a substantial influence on the *GPL* weight fraction and geometry. Furthermore, "when the *GPL* width-to-thickness ratio is higher than" 10^3, the influence of *GPL* geometry tends to be significantly less evident.
- The nanocomposite beam, while reinforced with *FG-X*, exhibits an extremely high vibration frequency, compared with the "*UD*, *FG-O* and *FG-A GPLRC* beams".
- For each *GPLs* shape, when the functionally graded graphene platelets used as reinforcing components, significantly increases the stiffness and strength of composite beams.

REFERENCES

1. Potts JR, Dreyer DR, Bielawski CW, Ruoff RS. Graphene-based polymer nanocomposites. Polymer. 2011;52(1):5–25. https://doi.org/ 10.1016/j.polymer.2010.11.042
2. Geim AK, Novoselov KS. The rise of graphene. Nature Mater. 2007;6(3):183–91. https://doi.org/ 10.1038/nmat1849
3. Maity N, Mandal A, Nandi AK. Hierarchical nanostructured polyaniline functionalized graphene/poly(vinylidene fluoride) composites for improved dielectric performances. Polymer. 2016;103:83–97. https://doi.org/ 10.1016/j.polymer.2016.09.048
4. Reif J, Rafiee J, Wang Z, Song H, Yu ZZ, Koratkar N. Enhanced Mechanical Properties of Nanocomposites at Low Graphene Content. ACS Nano. 2009;3(12):3884–90. https://doi.org/ 10.1021/nn9010472
5. Kundalwal SI, Shingare KB, Rathi A. Effect of flexoelectricity on the electromechanical response of graphene nanocomposite beam. Int J Mech Mater Des. 2019;15(3):447–70. https://doi.org/ 10.1007/s10999-018-9417-6
6. Wu H, Yang J, Kitipornchai S. Dynamic instability of functionally graded multilayer graphene nanocomposite beams in thermal environment. Composite Structures. 2017;162:244–54. https://doi.org/ 10.1016/j.compstruct.2016.12.001
7. Qaderi S, Ebrahimi F, Seyfi A. An investigation of the vibration of multilayer composite beams reinforced by graphene platelets resting on two parameter viscoelastic foundation. SN Appl Sci. 2019;1(5):399. https://doi.org/ 10.1007/s42452-019-0252-7
8. Feng C, Kitipornchai S, Yang J. Nonlinear bending of polymer nanocomposite beams reinforced with non-uniformly distributed graphene platelets (GPLs). Composites Part B: Engineering. 2017;110:132–40. https://doi.org/ 10.1016/j.compositesb.2016.11.024
9. Reza Barati M, Zenkour AM. Post-buckling analysis of refined shear deformable graphene platelet reinforced beams with porosities and geometrical imperfection. Composite Structures. 2017;181:194–202. https://doi.org/ 10.1016/j.compstruct.2017.08.082
10. Song M, Kitipornchai S, Yang J. Free and forced vibrations of functionally graded polymer composite plates reinforced with graphene nanoplatelets. Composite Structures. 2017;159:579–88. https://doi.org/ 10.1016/j.compstruct.2016.09.070
11. Zhou C, Zhang Z, Zhang J, Fang Y, Tahouneh V. Vibration analysis of FG porous rectangular plates reinforced by graphene platelets. Steel and Composite Structures. 2020;34(2):215–26. https://doi.org/ 10.12989/SCS.2020.34.2.215
12. Sobhy M, Zenkour AM. Vibration analysis of functionally graded graphene platelet-reinforced composite doubly-curved shallow shells on elastic foundations. Steel and Composite Structures. 2019;33(2):195–208. https://doi.org/ 10.12989/SCS.2019.33.2.195
13. Ganapathi M, Anirudh B, Anant C, Polit O. Dynamic characteristics of functionally graded graphene reinforced porous nanocomposite curved beams based on trigonometric shear deformation theory with thickness stretch effect. Mechanics of Advanced Materials and Structures. 2021;28(7):741–52. https://doi.org/ 10.1080/15376494.2019.1601310
14. Mazari MY, Hamza B, Dehbi F, Cheikh A, Saimi A, Bensaid I. Hybrid Galerkin-machine learning approach for dynamic analysis of nanocomposite beams under thermal effects. Mechanics Based Design of Structures and Machines. 2025;1–18. https://doi.org/ 10.1080/15397734.2025.2550531
15. Mazari MY, Hamza B, Slamene A, Dehbi F, Bensaid I, Mokhtari M. Integrating machine learning with vibration analysis for graphene platelet nanocomposite beams subjected to magnetic loading. Mechanics of Advanced Materials and Structures. 2025;1–11. https://doi.org/ 10.1080/15376494.2025.2476785
16. Wang Z, Chen S huan, Han W. The static shape control for intelligent structures. Finite Elements in Analysis and Design. 1997;26(4): 303-14. https://doi.org/ 10.1016/S0168-874X(97)00086-3
17. Hou W, Zheng Y, Guo W, Pengcheng G. Piezoelectric vibration energy harvesting for rail transit bridge with steel-spring floating slab track system. Journal of Cleaner Production. 2021;291:125283. https://doi.org/ 10.1016/j.jclepro.2020.125283
18. El Harti K, Rahmoune M, Sanbi M, Saadani R, Bentaleb M, Rahmoune M. Dynamic control of Euler Bernoulli FG porous beam under thermal loading with bonded piezoelectric materials. Ferroelectrics. 2020;558(1):104–16. https://doi.org/ 10.1080/00150193.2020.1735895
19. Zenkour AM, Aljadani MH. Buckling analysis of actuated functionally graded piezoelectric plates via a quasi-3D refined theory. Mechanics of Materials. 2020;151:103632. https://doi.org/ 10.1016/j.mechmat.2020.103632
20. Alazwari MA, Zenkour AM, Sobhy M. Hygrothermal Buckling of Smart Graphene/Piezoelectric Nanocomposite Circular Plates on an Elastic Substrate via DQM. Mathematics. 2022;10(15):2638. https://doi.org/ 10.3390/math10152638
21. Chen Q, Zheng S, Li Z, Zeng C. Size-dependent free vibration analysis of functionally graded porous piezoelectric sandwich nanobeam reinforced with graphene platelets with consideration of flexoelectric effect. Smart Mater Struct. 2021;30(3):035008. https://doi.org/ 10.1088/1361-665X/abd963
22. Sobhy M, Al Mukahal FHH. Analysis of Electromagnetic Effects on Vibration of Functionally Graded GPLs Reinforced Piezoelectromagnetic Plates on an Elastic Substrate. Crystals. 2022;12(4):487. https://doi.org/ 10.3390/cryst12040487

23. Mao JJ, Zhang W. Buckling and post-buckling analyses of functionally graded graphene reinforced piezoelectric plate subjected to electric potential and axial forces. Composite Structures. 2019;216:392–405. https://doi.org/ 10.1016/j.compstruct.2019.02.095
24. Liang Y, Zheng S, Wang H, Chen D. Nonlinear isogeometric analysis of axially functionally graded graphene platelet-reinforced composite curved beams. Composite Structures. 2024;330:117871. https://doi.org/ 10.1016/j.compstruct.2023.117871
25. Zhang X, Zhao X, Li Y, Wang H, Zheng S. Effect of flexoelectricity on the nonlinear static and dynamic response of functionally graded porous graphene platelets-reinforced composite plates integrated with piezoelectric layers. Int J Mech Mater Des. 2025;21(4):877–903. https://doi.org/ 10.1007/s10999-025-09765-5
26. Houalef IE, Bensaid I, Saimi A, Cheikh A. Free Vibration Analysis of Functionally Graded Carbon Nanotube-Reinforced Higher Order Refined Composite Beams Using Differential Quadrature Finite Element Method. TECM [Internet]. 2023 [cited 2025 Oct 14]. https://doi.org/ 10.13052/ejcm2642-2085.3143
27. Yang J, Wu H, Kitipornchai S. Buckling and postbuckling of functionally graded multilayer graphene platelet-reinforced composite beams. Composite Structures. 2017;161:111–8. https://doi.org/ 10.1016/j.compstruct.2016.11.048
28. Kundalwal SI. Review on micromechanics of nano- and micro-fiber reinforced composites. Polymer Composites. 2018;39(12):4243–74. https://doi.org/ 10.1002/pc.24569
29. Gupta M, Ray MC, Patil ND, Kundalwal SI. Dynamic modelling and analysis of smart carbon nanotube-based hybrid composite beams: Analytical and finite element study. Proceedings of the Institution of Mechanical Engineers, Part L: Journal of Materials: Design and Applications. 2021;235(10):2185–206. https://doi.org/ 10.1177/14644207211019773
30. Nebab M, Dahmane M, Belqassim A, Atmane HA, Bernard F, Benadouda M, et al. Fundamental frequencies of cracked FGM beams with influence of porosity and Winkler/Pasternak/Kerr foundation support using a new quasi-3D HSDT. Mechanics of Advanced Materials and Structures. 2024;31(28):10639–51. https://doi.org/ 10.1080/15376494.2023.2294371
31. Djilali Djebbour K, Mokhtar N, Hassen AA, Alghanmi RA, Hadji L, Riadh B. An enhanced quasi-3D HSDT for free vibration analysis of porous FG-CNT beams on a new concept of orthotropic VE-foundations. Mechanics of Advanced Materials and Structures. 2025;32(5):893–909. https://doi.org/ 10.1080/15376494.2024.2356728
32. Alsebai F, Al Mukahal FHH, Sobhy M. Semi-Analytical Solution for Thermo-Piezoelectric Bending of FG Porous Plates Reinforced with Graphene Platelets. Mathematics. 2022;10(21):4104. https://doi.org/ 10.3390/math10214104
33. Sobhy M, Abazid MA, Al Mukahal FH. Electro-thermal buckling of FG graphene platelets-strengthened piezoelectric beams under humid conditions. Advances in Mechanical Engineering. 2022;14(4):168781322210910. https://doi.org/ 10.1177/16878132221091005
34. Ahmed S, Abdelhamid H, Ismail B, Ahmed F. An Differential Quadrature Finite Element and the Differential Quadrature Hierarchical Finite Element Methods for the Dynamics Analysis of on Board Shaft. TECM [Internet]. 2021 [cited 2025 Oct 14]. https://doi.org/ 10.13052/ejcm1779-7179.29461
35. Dahmane M, Benadouda M, Fellah A, Saimi A, Hassen AA, Bensaid I. Porosities-dependent wave propagation in bi-directional functionally graded cantilever beam with higher-order shear model. Mechanics of Advanced Materials and Structures. 2024;31(26):8018–28. https://doi.org/ 10.1080/15376494.2023.2253546
36. Bensaid I, Saimi A, Civalek Ö. Effect of two-dimensional material distribution on dynamic and buckling responses of graded ceramic-metal higher order beams with stretch effect. Mechanics of Advanced Materials and Structures. 2024;31(8):1760–76. https://doi.org/ 10.1080/15376494.2022.2142342
37. Şimşek M. Fundamental frequency analysis of functionally graded beams by using different higher-order beam theories. Nuclear Engineering and Design. 2010;240(4):697–705. https://doi.org/ 10.1016/j.nucengdes.2009.12.013

Mohammed Yassine Mazari: https://orcid.org/0009-0004-5592-0151

Ismail Bensaid: https://orcid.org/0000-0003-4316-0648

Ahmed Saimi: https://orcid.org/0000-0002-3722-2526

Abdelmadjid Cheikh: https://orcid.org/0000-0001-5876-2786

Ihab Eddine Houalef: https://orcid.org/0000-0001-9130-9422

Billel Hamza: https://orcid.org/0009-0005-3098-6143

Appendix A. Detailed Equations

$$U_b = \frac{1}{2}b\int_0^l \begin{pmatrix} I_1\frac{du}{dx}\frac{du}{dx} - 2I_2\frac{du}{dx}\frac{d^2w_b}{dx^2} - 2I_3\frac{du}{dx}\frac{d^2w_S}{dx^2} \\ +2I_4\frac{d^2w_b}{dx^2}\frac{d^2w_s}{dx^2} \\ +I_5\frac{d^2w_b}{dx^2}\frac{d^2w_b}{dx^2} + I_6\frac{d^2w_s}{dx^2}\frac{d^2w_s}{dx^2} + I_7w_z^2 + 2I_8\frac{du}{dx}w_z \\ -2I_9\frac{d^2w_b}{dx^2}w_z \\ -2I_{10}\frac{d^2w_s}{dx^2}w_z + I_{11}\left(\frac{d^2w_s}{dx^2}\frac{d^2w_s}{dx^2} + \frac{d^2w_z}{dx^2}\frac{d^2w_z}{dx^2} + 2\frac{dw_s}{dx}\frac{dw_z}{dx}\right) \\ +I_{12}\frac{du}{dx}\psi - I_{13}\frac{d^2w_b}{dx^2}\psi - I_{14}\frac{d^2w_s}{dx^2}\psi + I_{15}w_z\psi \\ -I_{16}\left(\frac{dw_s}{dx}\frac{d\psi}{dx} + \frac{dw_z}{dx}\frac{d\psi}{dx}\right) - I_{17}\psi\psi - I_{18}\frac{d\psi}{dx}\frac{d\psi}{dx} \end{pmatrix} dx \tag{A.1}$$

$$\begin{cases} \{I_{1:7}\} = b\int_{-\frac{h}{2}}^{\frac{h}{2}} Q_{11}\left(1, z, f, zf, z^2, f^2, \left(\frac{dg}{dz}\right)^2\right)dz \\ \{I_{8:10}\} = b\int_{-\frac{h}{2}}^{\frac{h}{2}} Q_{11}\frac{dg}{dz}(1, z, f)dz \\ \{I_{11}\} = b\int_{-\frac{h}{2}}^{\frac{h}{2}} Q_{55}g^2dz \\ \{I_{12:14}\} = \frac{b\pi}{h}A_{31}\int_{-\frac{h}{2}}^{\frac{h}{2}} sin\left(\frac{\pi z}{h}\right)(1, z, f)dz \end{cases} \tag{A.2}$$

$$\begin{cases} \{I_{15}\} = \frac{b\pi}{h}A_{33}\int_{-\frac{h}{2}}^{\frac{h}{2}} \frac{dg}{dz}sin\left(\frac{\pi z}{h}\right)dz \\ \{I_{16}\} = bA_{15}\int_{-\frac{h}{2}}^{\frac{h}{2}} gcos\left(\frac{\pi z}{h}\right)dz \\ \{I_{17}\} = bs_{33}\left(\frac{\pi}{h}\right)^2\int_{-\frac{h}{2}}^{\frac{h}{2}} sin^2\left(\frac{\pi z}{h}\right)dz \\ \{I_{18}\} = bs_{11}\int_{-\frac{h}{2}}^{\frac{h}{2}} cos^2\left(\frac{\pi z}{h}\right)dz \end{cases} \tag{A.3}$$

$$U_b = \frac{1}{2}b\begin{bmatrix} I_1\left[Q^T\bar{A}^{(1)^T}\bar{C}\bar{A}^{(1)}Q\right]u^2 - 2I_2\left[Q^T\bar{A}^{(1)^T}\bar{C}\bar{A}^{(2)}Q\right]uw_b \\ -2I_3\left[Q^T\bar{A}^{(1)^T}\bar{C}\bar{A}^{(2)}Q\right]uw_s + 2I_4\left[Q^T\bar{A}^{(2)^T}\bar{C}\bar{A}^{(2)}Q\right]w_bw_s \\ +I_5\left[Q^T\bar{A}^{(2)^T}\bar{C}\bar{A}^{(2)}Q\right]w_bw_b + I_6\left[Q^T\bar{A}^{(2)^T}\bar{C}\bar{A}^{(2)}Q\right]w_sw_s + I_7[Q^T\bar{C}Q]w_z^2 \\ +2I_8\left[\bar{Q}^T\bar{A}^{(1)^T}\bar{C}Q\right]uw_z - 2I_9\left[\bar{Q}^{-T}\bar{A}^{(2)^T}\bar{C}\bar{Q}^{-1}\right]w_bw_z \\ -2I_{10}\left[\bar{Q}^{-T}\bar{A}^{(2)^T}\bar{C}\bar{Q}^{-1}\right]w_sw_z + I_{11}\begin{pmatrix}\left[\bar{Q}^{-T}\bar{A}^{(2)^T}\bar{C}\bar{A}^{(2)}\bar{Q}^{-1}\right]w_sw_s \\ +\left[\bar{Q}^{-T}\bar{A}^{(2)^T}\bar{C}\bar{A}^{(2)}\bar{Q}^{-1}\right]w_zw_z \\ +2\left[\bar{Q}^{-T}\bar{A}^{(1)^T}\bar{C}\bar{A}^{(1)}\bar{Q}^{-1}\right]w_sw_z\end{pmatrix} \\ +I_{12}\left[\bar{Q}^{-T}\bar{A}^{(1)^T}\bar{C}\bar{Q}^{-1}\right]u\psi - I_{13}\left[\bar{Q}^{-T}\bar{A}^{(2)^T}\bar{C}\bar{Q}^{-1}\right]w_b\psi \\ -I_{14}\left[\bar{Q}^{-T}\bar{A}^{(2)^T}\bar{C}\bar{Q}^{-1}\right]w_s\psi + I_{15}[\bar{Q}^{-T}\bar{C}\bar{Q}^{-1}]w_z\psi \\ -I_{16}\left(\left[\bar{Q}^{-T}\bar{A}^{(1)^T}\bar{C}\bar{A}^{(1)}\bar{Q}^{-1}\right]w_s\psi + \left[\bar{Q}^{-T}\bar{A}^{(1)^T}\bar{C}\bar{A}^{(1)}\bar{Q}^{-1}\right]w_z\psi\right) \\ -I_{17}[\bar{Q}^{-T}\bar{C}\bar{Q}^{-1}]\psi\psi - I_{18}\left[\bar{Q}^{-T}\bar{A}^{(1)^T}\bar{C}\bar{A}^{(1)}\bar{Q}^{-1}\right]\psi\psi \end{bmatrix} \tag{A.4}$$

$$K_b = \frac{1}{2}b\begin{bmatrix} J_1[\bar{Q}^{-T}\bar{C}\bar{Q}^{-1}]\left(\dot{u}^2 + \dot{w}_b{}^2 + \dot{w}_s{}^2 + 2\dot{w}_b\dot{w}_s\right) - 2J_2\left[\bar{Q}^{-T}\bar{C}\bar{A}^{(1)}\bar{Q}^{-1}\right]\dot{u}\dot{w}_b \\ -2J_3\left[\bar{Q}^{-T}\bar{C}\bar{A}^{(1)}\bar{Q}^{-1}\right]\dot{u}\dot{w}_s + 2J_4\left[\bar{Q}^{-T}\bar{A}^{(1)^T}\bar{C}\bar{A}^{(1)}\bar{Q}^{-1}\right]\dot{w}_b\dot{w}_s \\ +J_5\left[\bar{Q}^{-T}\bar{A}^{(1)^T}\bar{C}\bar{A}^{(1)}\bar{Q}^{-1}\right]\dot{w}_b{}^2 + J_6\left[\bar{Q}^{-T}\bar{A}^{(1)^T}\bar{C}\bar{A}^{(1)}\bar{Q}^{-1}\right]\dot{w}_s{}^2 \\ +J_7[\bar{Q}^{-T}\bar{C}\bar{Q}^{-1}]\dot{w}_z{}^2 + 2J_8[\bar{Q}^{-T}\bar{C}\bar{Q}^{-1}](\dot{w}_b\dot{w}_z + \dot{w}_s\dot{w}_z) \end{bmatrix} \tag{A.5}$$

$$\begin{cases} [M]_{11} = J_1[\bar{Q}^{-T}\bar{C}\bar{Q}^{-1}] \\ [M]_{12} = -J_2\left[\bar{Q}^{-T}\bar{C}\bar{A}^{(1)}\bar{Q}^{-1}\right] \\ [M]_{13} = J_3\left[\bar{Q}^{-T}\bar{C}\bar{A}^{(1)}\bar{Q}^{-1}\right] \\ [M]_{22} = J_1[\bar{Q}^{-T}\bar{C}\bar{Q}^{-1}] + J_5\left[\bar{Q}^{-T}\bar{A}^{(1)^T}\bar{C}\bar{A}^{(1)}\bar{Q}^{-1}\right] \\ [M]_{23} = J_1[\bar{Q}^{-T}\bar{C}\bar{Q}^{-1}] - J_4\left[\bar{Q}^{-T}\bar{A}^{(1)^T}\bar{C}\bar{A}^{(1)}\bar{Q}^{-1}\right] \\ [M]_{24} = J_8[\bar{Q}^{-T}\bar{C}\bar{Q}^{-1}] \\ [M]_{33} = J_1[\bar{Q}^{-T}\bar{C}\bar{Q}^{-1}] + J_6\left[\bar{Q}^{-T}\bar{A}^{(1)^T}\bar{C}\bar{A}^{(1)}\bar{Q}^{-1}\right] \\ [M]_{34} = J_8[\bar{Q}^{-T}\bar{C}\bar{Q}^{-1}] \\ [M]_{44} = J_7[\bar{Q}^{-T}\bar{C}\bar{Q}^{-1}] \end{cases} \tag{A.6}$$

$$\begin{bmatrix} [K]_{11} & [K]_{12} & [K]_{13} & [K]_{14} & [K]_{15} \\ & [K]_{22} & [K]_{23} & [K]_{24} & [K]_{25} \\ & & [K]_{33} & [K]_{34} & [K]_{35} \\ & & & [K]_{44} & [K]_{45} \\ Sym & & & & [K]_{55} \end{bmatrix} - \omega^2 \begin{bmatrix} [M]_{11} & [M]_{12} & [M]_{13} & [0] & [0] \\ & [M]_{22} & [M]_{23} & [M]_{24} & [0] \\ & & [M]_{33} & [M]_{34} & [0] \\ & & & [M]_{44} & [0] \\ Sym & & & & [0] \end{bmatrix} \begin{Bmatrix} u_0(t) \\ w_b(t) \\ w_s(t) \\ w_z(t) \\ \zeta(t) \end{Bmatrix} = [0] \tag{A.7}$$

$$\begin{cases} [M]_{11} = J_1[\bar{Q}^{-T}\bar{C}\bar{Q}^{-1}] \\ [M]_{12} = -J_2\left[\bar{Q}^{-T}\bar{C}\bar{A}^{(1)}\bar{Q}^{-1}\right] \\ [M]_{13} = J_3\left[\bar{Q}^{-T}\bar{C}\bar{A}^{(1)}\bar{Q}^{-1}\right] \\ [M]_{22} = J_1[\bar{Q}^{-T}\bar{C}\bar{Q}^{-1}] + J_5\left[\bar{Q}^{-T}\bar{A}^{(1)^T}\bar{C}\bar{A}^{(1)}\bar{Q}^{-1}\right] \\ [M]_{23} = J_1[\bar{Q}^{-T}\bar{C}\bar{Q}^{-1}] - J_4\left[\bar{Q}^{-T}\bar{A}^{(1)^T}\bar{C}\bar{A}^{(1)}\bar{Q}^{-1}\right] \\ [M]_{24} = J_8[\bar{Q}^{-T}\bar{C}\bar{Q}^{-1}] \\ [M]_{33} = J_1[\bar{Q}^{-T}\bar{C}\bar{Q}^{-1}] + J_6\left[\bar{Q}^{-T}\bar{A}^{(1)^T}\bar{C}\bar{A}^{(1)}\bar{Q}^{-1}\right] \\ [M]_{34} = J_8[\bar{Q}^{-T}\bar{C}\bar{Q}^{-1}] \\ [M]_{44} = J_7[\bar{Q}^{-T}\bar{C}\bar{Q}^{-1}] \end{cases} \tag{A.8}$$

$$\begin{cases} [K]_{11} = I_1\left[\bar{Q}^{-T}\bar{A}^{(1)^T}\bar{C}\bar{A}^{(1)}\bar{Q}^{-1}\right] \\ [K]_{12} = -I_2\left[\bar{Q}^{-T}\bar{A}^{(1)^T}\bar{C}\bar{A}^{(2)}\bar{Q}^{-1}\right] \\ [K]_{13} = -I_3\left[\bar{Q}^{-T}\bar{A}^{(1)^T}\bar{C}\bar{A}^{(2)}\bar{Q}^{-1}\right] \\ [K]_{14} = I_8\left[\bar{Q}^{-T}\bar{A}^{(1)^T}\bar{C}\bar{Q}^{-1}\right] \\ [K]_{15} = I_{12}\left[\bar{Q}^{-T}\bar{A}^{(1)^T}\bar{C}\bar{Q}^{-1}\right] \\ [K]_{22} = I_5\left[\bar{Q}^{-T}\bar{A}^{(2)^T}\bar{C}\bar{A}^{(2)}\bar{Q}^{-1}\right] - N_{TOT}\left[\bar{Q}^{-T}\bar{A}^{(1)^T}\bar{C}\bar{A}^{(1)}\bar{Q}^{-1}\right] \\ [K]_{23} = I_4\left[\bar{Q}^{-T}\bar{A}^{(2)^T}\bar{C}\bar{A}^{(2)}\bar{Q}^{-1}\right] - N_{TOT}\left[\bar{Q}^{-T}\bar{A}^{(1)^T}\bar{C}\bar{A}^{(1)}\bar{Q}^{-1}\right] \\ [K]_{24} = -I_9\left[\bar{Q}^{-T}\bar{A}^{(2)^T}\bar{C}\bar{Q}^{-1}\right] - N_{TOT}g\left[\bar{Q}^{-T}\bar{A}^{(1)^T}\bar{C}\bar{A}^{(1)}\bar{Q}^{-1}\right] \\ [K]_{25} = I_{13}\left[\bar{Q}^{-T}\bar{A}^{(2)^T}\bar{C}\bar{Q}^{-1}\right] \\ [K]_{33} = I_6\left[\bar{Q}^{-T}\bar{A}^{(2)^T}\bar{C}\bar{A}^{(2)}\bar{Q}^{-1}\right] + I_{11}\left[\bar{Q}^{-T}\bar{A}^{(1)^T}\bar{C}\bar{A}^{(1)}\bar{Q}^{-1}\right] - N_{TOT}\left[\bar{Q}^{-T}\bar{A}^{(1)^T}\bar{C}\bar{A}^{(1)}\bar{Q}^{-1}\right] \\ [K]_{34} = -I_{10}\left[\bar{Q}^{-T}\bar{A}^{(2)^T}\bar{C}\bar{Q}^{-1}\right] + I_{11}\left[\bar{Q}^{-T}\bar{A}^{(1)^T}\bar{C}\bar{A}^{(1)}\bar{Q}^{-1}\right] - N_{TOT}g\left[\bar{Q}^{-T}\bar{A}^{(1)^T}\bar{C}\bar{A}^{(1)}\bar{Q}^{-1}\right] \\ [K]_{35} = -I_{14}\left[\bar{Q}^{-T}\bar{A}^{(2)^T}\bar{C}\bar{Q}^{-1}\right] - I_{16}\left[\bar{Q}^{-T}\bar{A}^{(1)^T}\bar{C}\bar{A}^{(1)}\bar{Q}^{-1}\right] \\ [K]_{44} = I_7[\bar{Q}^{-T}\bar{C}\bar{Q}^{-1}] + I_{11}\left[\bar{Q}^{-T}\bar{A}^{(1)^T}\bar{C}\bar{A}^{(1)}\bar{Q}^{-1}\right] - N_{TOT}g^2\left[\bar{Q}^{-T}\bar{A}^{(1)^T}\bar{C}\bar{A}^{(1)}\bar{Q}^{-1}\right] \\ [K]_{45} = I_{15}[\bar{Q}^{-T}\bar{C}\bar{Q}^{-1}] - I_{16}\left[\bar{Q}^{-T}\bar{A}^{(1)^T}\bar{C}\bar{A}^{(1)}\bar{Q}^{-1}\right] \\ [K]_{55} = -I_{17}[\bar{Q}^{-T}\bar{C}\bar{Q}^{-1}] - I_{18}\left[\bar{Q}^{-T}\bar{A}^{(1)^T}\bar{C}\bar{A}^{(1)}\bar{Q}^{-1}\right] \end{cases} \tag{A.9}$$